




# The Timeline of Early Lunar Bombardment Constrained by the Evolving Distributions of Differently Aged Melt

Tiantian Liu<sup>1</sup> , Greg Michael<sup>2</sup>, and Kai Wünnemann<sup>1,2</sup><sup>1</sup> Museum für Naturkunde, Leibniz Institute for Evolution and Biodiversity Science, D-10115 Berlin, Germany; [tiantian.liu@mfn.berlin](mailto:tiantian.liu@mfn.berlin)<sup>2</sup> Freie Universität Berlin, Malteserstr., 74-100, D-12249 Berlin, Germany

Received 2023 February 5; revised 2023 June 19; accepted 2023 June 20; published 2023 July 31

## Abstract

The timeline of the early lunar bombardment remains unclear. The bombardment rate as a function of time is commonly modeled by three types of shapes: tail-end, sawtooth, and terminal cataclysm. Differently aged melt records the occurrence time of impact events and thus is crucial for constraining the timeline of the early lunar bombardment. Based on a spatially resolved numerical model, we simulate the evolving distribution of differently aged melt with a long-term impact mixing, where different shapes of impact rate function are considered. We compare the outcome of melt age distribution from different scenarios with the actual data from the lunar meteorites and the returned samples. The results suggest that, if the present data are representative of the melt age distribution on the Moon, the shape of the impact rate function is more likely comparable to the tail-end over the sawtooth and the terminal cataclysm, with the terminal cataclysm being least likely. In addition, using state-of-the-art U–Pb dating techniques, more abundant ancient basin melt is likely to be found in returned samples.

*Unified Astronomy Thesaurus concepts:* [Earth-moon system \(436\)](#); [Lunar craters \(949\)](#); [Impact gardening \(2299\)](#); [Monte Carlo methods \(2238\)](#); [Meteorites \(1038\)](#)

## 1. Introduction

The early bombardment history of the Moon provides fundamental constraints on the final stages of planetary accretion, the period that is usually referred to as late accretion from 4.5 to 3.8 billion years ago. The impactor flux during this stage was much more intense than it is in the present day. The corresponding impact events were recorded after crystallization of the lunar magma ocean and formation of the crust, such that they could be preserved as craters and basins. The existence of the intensive bombardment during late accretion is generally accepted, but the overall timeline, i.e., the impact rate, and how it evolved with time are still disputed.

One view is the terminal cataclysm or the late heavy bombardment. The idea was proposed on the geochronological ground, where the K–Ar and Rb–Sr isotopic datings at the Apollo samples present a prevalence age of  $\sim 3.9$  Ga and virtually absent signatures for the older ages. It led to the hypothesis of a spike in the impactor flux at  $\sim 3.9$  Ga (Tera et al. 1973, 1974; Cohen 2000; Norman et al. 2006), which has been used to argue for a dramatic reorganization in solar system architecture at that time (Tsiganis et al. 2005; Marchi et al. 2012).

The opposite view is the accretion tail-end. In this view, the impact rate has decayed monotonically since the formation of the terrestrial planets ( $\sim 4.5$  Ga ago), and the high concentration of 3.9 Ga impact ages was caused by age resetting (Boehnke & Harrison 2016) or sampling biases at Apollo landing sites caused by abundant impactites in the ejecta of the 3.9 Ga old Imbrium basin (Haskin et al. 1998; Hartmann 2003; Chapman et al. 2007; Fernandes et al. 2013; Michael et al. 2018; Schaeffer & Schaeffer 1977; Norman et al. 2010). The

mechanism of this scenario was suggested as being related to the gradually removed planetesimals leftover from planet accretion by dynamical and collisional mechanisms. The work of Neukum and Ivanov sustains this scenario (Neukum 1983; Ivanov 2001; Michael & Neukum 2010).

Another view, a sawtooth profile, is a hybrid scenario derived from the modeling of the early solar system evolution by Morbidelli et al. (2012). They refer to the accretion tail-end and terminal cataclysm as two endmembers and infer that the impact rate of the early bombardment is intermediate between these two endmembers. The profile displays an uptick in the impact flux  $\sim 4.1$  Ga ago. The impact flux at the beginning of this cataclysm was 5–10 times higher than the preceding period; the rate of the older bombardment declined slowly and adhered close to tail-end models. The  $>4.1$  Ga bombardments are assumed to be caused by the strike of leftover planetesimals, whereas the  $<4.1$  Ga late bombardments are stimulated by the giant planet migration.

The early bombardment history is, in principle, recorded by the large impact basins. Due to the low rates of surface modification, the Moon is the body in the inner solar system that has best retained the traces of impact basins. However, interpreting the lunar bombardment history as recorded by the impact basins has been found to be complicated owing to the difficulty in recognizing ancient basins. The surface expressions of old basins tend to be subtler than younger basins. The ancient impact basins that formed just after the main crystallization phase of lunar magma ocean likely failed to produce long-lasting detectable structures (Zhu et al. 2019). In addition, the surface units with well-determined radiometric ages are insufficient, and they are mostly younger than 3.9 Ga (Stöffler & Ryder 2001; Robbins 2014). Even if some of these datings are derived from basin-forming events, they are only available for the age determination of a few young basins (Stöffler 2006).

Impact melt, the product of a hypervelocity cratering process, provides essential evidence for understanding the timeline of the early bombardment. Impact-induced heating



Original content from this work may be used under the terms of the [Creative Commons Attribution 4.0 licence](#). Any further distribution of this work must maintain attribution to the author(s) and the title of the work, journal citation and DOI.

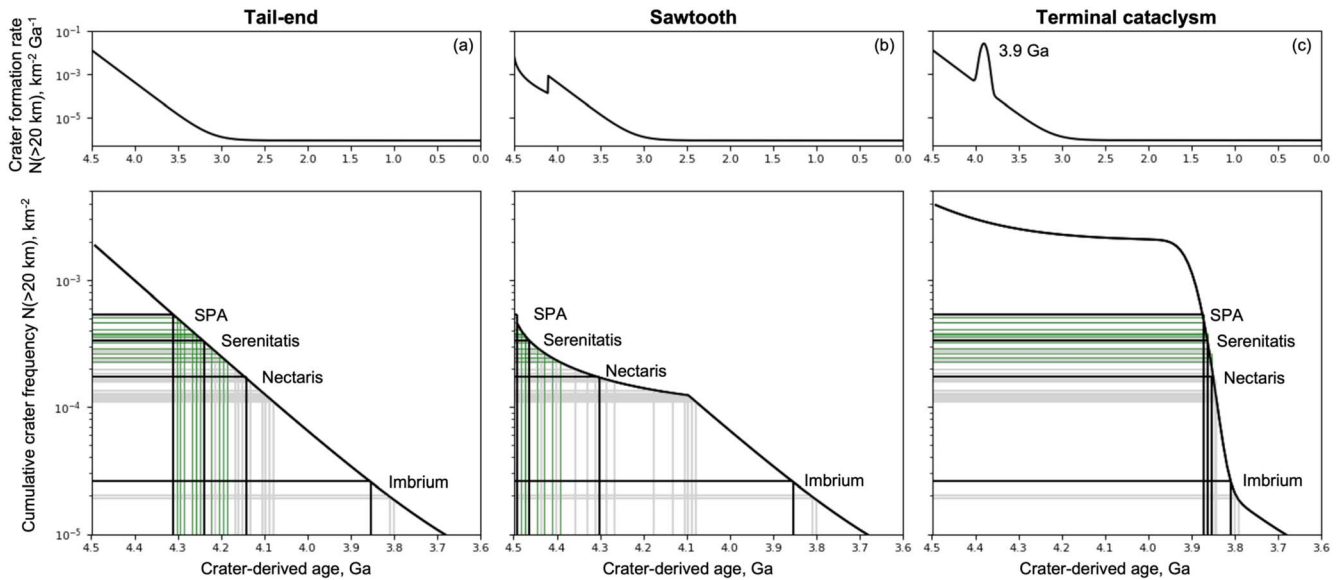


**Figure 1.** Three different scenarios of the early bombardment history, where the impact rate functions are shown above and the plots below are in cumulative form. The typical Neukum impact rate (panel (a)) is taken to represent the tail-end scenario. The impact rate of the terminal cataclysm scenario (panel (c)) is the same as the tail-end but contains an addition of a “cataclysmic peak” at 3.9 Ga. The impact rate of the sawtooth scenario (panel (b)) is directly adopted from Morbidelli et al. (2012): for  $t < 4.1$  Ga,  $dN_{20}/dt = 2.7 \times 10^{-16} e^{6.93t} + 5.9 \times 10^{-7}$ ; for  $t > 4.1$  Ga,  $dN_{20}/dt = 2.5 \times 10^{-2} e^{-1 - 4.5 - t/0.003} \wedge 0.34$ , where the time  $t$  is measured in Ga. In the cumulative forms, the plausible distribution of time points for basin-forming events as predicted from  $N(20)$  crater densities (Orgel et al. 2018) is indicated by gray data. The four largest basin events, South Pole–Aitken, Serenitatis, Nectaris, and Imbrium, are labeled and indicated with black lines. The green lines indicate the calculated crater-derived ages of newly detected pre-Nectarian basins (Conrad et al. 2018).

melts some of the target materials, resetting their isotopic time clock and thus recording the formation time of the corresponding impact event. In both the lunar meteorites and the returned samples, abundant impact melt products have been found. These melt products should have provided ground-truth references for constraining the impact rate of the early bombardment. However, the interpretation of the sample origin is found to be difficult, and hence its link to the basins is ambiguous. This mainly results from the unceasing mixing of different components caused by numerous subsequent impacts. Each impact event generates new melt with an age of its occurrence time while depleting some old melts by resetting their age. The excavated materials carrying both some new melt and existing components are dispersed over a wide range burying the old materials. Such long-term impact mixing (melting/remelting, excavating, burying and re-excavating) constantly changes the material distribution, resulting in a complicated melt age distribution in the present day. Liu et al. (2020a) built a spatially resolved numerical model to investigate the effect of a long sequence of impacts on melt diffusion considering a tail-end impact rate only. They estimated the distribution of differently aged melt over the Moon and constrained the origin of the impact melt contained in lunar samples. In this study, we expand the previous study by considering different possible shapes of the impact rate function, with the aim to further distinguish which timeline is more consistent with the data provided by the samples.

In Section 2, the model mechanism is described. Using this model, we estimate the global and regional distribution of differently aged melt while considering three forms of the early bombardment timeline (Section 3). In addition, due to the importance of the considered basin inventory, we present how the varying number of basin-forming events affects the melt age distribution. By comparing the modeling results with the isotopic datings of samples, we summarized the model-

constrained knowledge on the impact rate of early bombardment. With this knowledge, we particularly analyze the abundance of Nectaris basin melt (Section 4) and pre-Nectarian melt (Section 5) in the returned samples. Identifying these ancient basin melts with constrained origins would provide crucial anchor points for the study of early bombardment.

## 2. Methods

Our impact mixing model, which allows for tracing the evolution of material age distribution with long-term bombardment, has been applied to different components such as impact melt, mare/highland materials, and different-sized fragments (Liu et al. 2020a, 2020b, 2022b). In this study, we focus on the impact melt but take different scenarios of the early bombardment rate into account. In this section, we describe the essential components of the model. More detailed explanations are contained in Appendix A.

### 2.1. Impact Mixing Model

We use the Monte Carlo method to simulate the cumulative impact mixing considering three scenarios of impact rate (tail-end, terminal cataclysm, and sawtooth). We choose the Neukum impact rate (Neukum 1983) to represent the tail-end scenario. The impact rate of the terminal cataclysm scenario is calculated by adding a prominent Gaussian peak at 3.9 Ga to the tail-end impact rate (Michael et al. 2018). The impact rate of the sawtooth scenario is directly adopted from Morbidelli et al. (2012). With the knowledge of lunar chronology and production functions (PFs; Neukum 1983), the sequence of impact events is generated for three different types of impact rate function (Figures 1 and A1). Only craters larger than 5 km are considered, and impact events of different sizes randomly occurred over the Moon in chronological sequence. For each impact, the processes of melting (remelting), excavation, and

ejecta deposition are simulated. Each impact would heat a certain amount of material, producing new melt with an age of its occurrence time. When an impact event occurs on preexisting melts, a fraction of these old melts are remelted, and their ages are reset to the occurrence time of the fresh impact.

The majority of the generated melt is distributed inside and near the crater cavities, and regions far away contain less generated melt (Melosh 1989; Liu et al. 2022a). In the ejecta, the thickness of both the total materials and the contained new melt is exponentially decreasing with the distance from the impact center, but due to the smaller decreasing rate of melt thickness, the melt concentration is increasing with distance. With the emplacement of the ejecta, the old melt on the surface would be buried to a greater depth. Ultimately, with the perpetual occurrence of randomly distributed impact events, the distribution of the differently aged melt becomes spatially varied, and the melt age distribution becomes distinct at different locations and depths.

The model starts with the formation of the oldest verified basin, South Pole–Aitken (SPA; Garrick-Bethell & Zuber 2009), and ends with the formation of the youngest impact where the present-day melt age distribution is obtained. The randomly distributed impact events cause various melt age distribution of regional areas. To get statistical results, for each impact rate scenario we repeat our Monte Carlo simulations 10 times with varying crater locations and sizes (Huang et al. 2017; Michael et al. 2018) for constant crater size–frequency distribution according to the crater PF (Figure A1). The average results of the multiple simulations are then taken for analysis.

## 2.2. Formation Sequence of Impact Basins

The total amount of the generated impact melt exponentially increases with the crater size (Cintala & Grieve 1998; Liu et al. 2022a). Thus, basin-size impacts are thought to be responsible for the vast majority of the existing impact melt. This melt and how it is distributed and subsequently mixed and displaced by following impacts are pivotal for the interpretation of ages derived from samples by linking them to certain impact events, thus understating the early bombardment history. The occurrence of basin-forming events in our model is not random but follows the inventory and stratigraphic age of known basins. The timing is calculated according to the  $N(20)$  crater densities measured by Orgel et al. (2018) using the chronology function according to the three different bombardment rates. Note that  $N(20)$  is the cumulative number of craters of size greater than or equal to diameter 20 km. We modify the value for the SPA basin to force it to be the oldest in the stratigraphic sequence (Stöffler 2006). To distinguish from the radioisotopic ages, the calculated basin ages are referred to as “crater-derived age” (Figure 1). In both the tail-end and sawtooth scenarios, the basin ages are scattered over a certain range, with the former from 4.3 to 3.8 Ga and the latter from 4.5 to 3.8 Ga. In the terminal cataclysm scenario, all the basins are formed in a short period around 3.85 Ga.

It should be mentioned that the calculated formation times of basins are taken as a plausible configuration of impact times but may not correspond to the accurate age of particular basins. Our goal is to understand the expected consequences of a given configuration in the record of returned lunar samples and meteorites and finally to compare the model record with the actual record to constrain the timeline of the bombardment

history. We are thus focusing on the statistical melt distribution, rather than the specific ages. Interpreting the origin of the specific age of lunar samples is beyond the scope of this paper.

## 3. Results

The modeling results are compared with the radioisotopic datings of lunar samples. However, there are uncertainties for both the isotopic datings and the crater-derived ages. The different isotopic systems have different closure temperatures, and hence for a given impact event (i.e., a certain heating event) they could have distinct responses affecting the determined isotopic ages. For instance, the K–Ar system has a relatively low closure temperature, and their time clock could be reset merely by losing argon caused by being hosted in a hot ejecta blanket or by impact shock (Fernandes et al. 2013; Boehnke et al. 2016). In contrast, due to the high close temperature of the U–Pb system, the required energy to reset its time clock is greater (Cherniak & Watson 2001). Overall, the statistics of K–Ar datings bias toward the young ages, whereas the U–Pb datings present more older ages. The uncertainty of crater-derived ages is derived not only from the applied chronology function but also from the identification of craters (Michael & Neukum 2010; Orgel et al. 2018). These uncertainties would result in different interpretations of impact rate in small time intervals but could not significantly change the general features of the bombardment timeline. Therefore, while making comparisons, for both the radioisotopic datings and the model-derived melt age distribution, we present only a broad picture, commenting on significant peaks.

### 3.1. Global Distribution

Whether a basin-forming event can leave a significant component of melt with the age of its formation time depends on the amount of its produced melt (i.e., the scale of the basin) relative to the total production of melt from smaller impacts at that time (i.e., the number of small impacts). Although the melt volume of a basin-scale impact event is several orders of magnitude greater than that of a single small impact (Cintala & Grieve 1998; Zhu et al. 2017; Liu et al. 2022a), due to the very large number of small impacts (Neukum 1983), their aggregated melt volume may be comparable to that of a basin-scale impact, especially in the uppermost layer, where the influence of small impact mixing is significantly enhanced (Liu et al. 2021). Assuming that 25% of the total basin melt is ejected and covers the surface (Liu et al. 2022a, Appendix A), a basin with a transient crater diameter of 300 km would have a comparable amount of melt in the near surface to that of  $\sim 10^5$  craters with a diameter of 10 km. In addition, the older the melt, the more likely that it is deeply buried by the ejecta of late-forming impact events. How much of the old melt remains in the near surface determines whether it can preserve distinct evidence in the impact records of the surface materials. The old basin melts would be deeply buried if there are large-scale impacts subsequently occurring nearby; otherwise, the small impacts would be able to dig them up.

The various impact rate functions result in different frequencies of small impacts (Figure A1) and distinct crater-derived ages of basins for the given  $N(20)$  values (Figure 1). Figure 2 presents the distribution of differently aged melt in the near surface considering various shapes of impact rate function. The most remarkable difference is the general distribution of



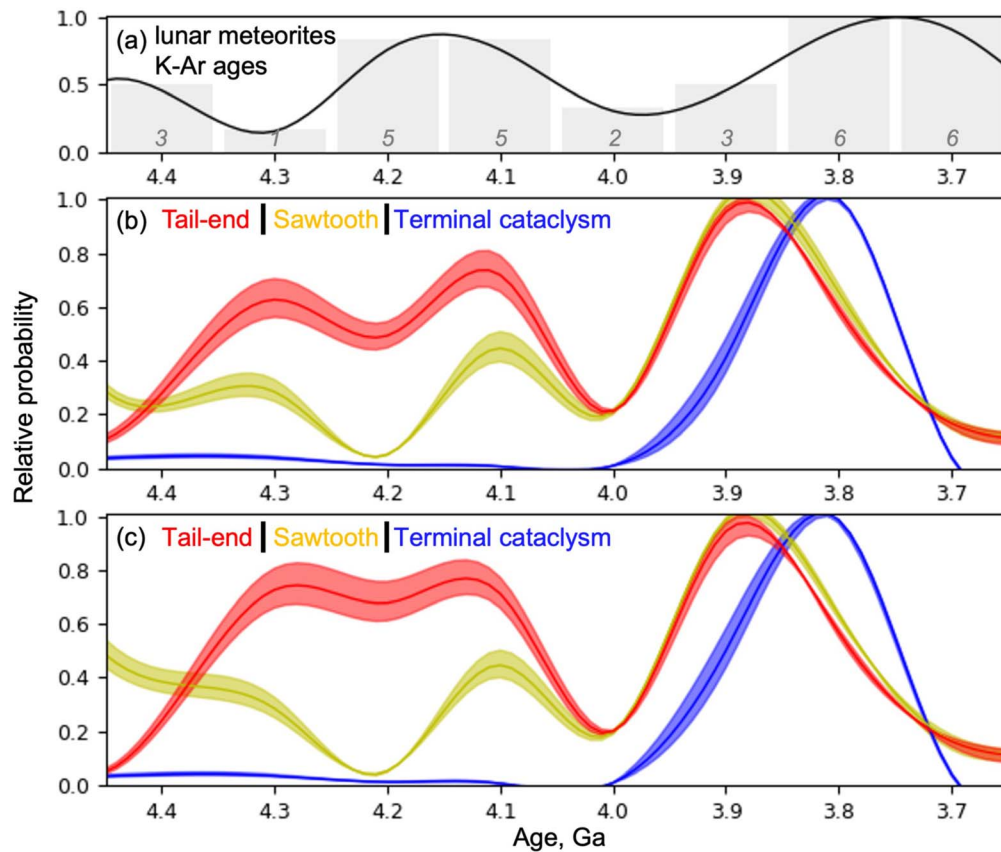


**Figure 2.** Globally average distribution of differently aged melt in the near surface. (a) K–Ar datings of lunar meteorites (Michael et al. 2018), where the black curve is the first-order spline interpolation of the gray histogram. The italic number indicates the number of datings. Panels (b) and (c) are the model-derived melt age distributions (top 5 m, comparable to the typical origin depth of lunar meteorites; Warren 1994) while considering the basin list of Orgel et al. (2018) and the addition of newly detected pre-Nectarian basins (Conrad et al. 2018), respectively. The considered basins in panel (c) are 12 more than in panel (b). The shaded areas indicate the standard deviation of the 10 times Monte Carlo simulations.

peaks. While both the tail-end and the sawtooth present three peaks at 3.9, 4.1, and 4.3 Ga, the terminal cataclysm results in only one prominent peak at around 3.8 Ga. Another significant difference is the probability relative to the most abundant melt (i.e., the prime peak). Compared to the tail-end scenario, the probability of 4.1 and 4.3 Ga melt is significantly smaller than the prime peak of 3.9 Ga in the sawtooth scenario.

The lunar meteorites represent samples from the upper few meters of the regolith (Vogt et al. 1991; Warren 1994) and probably originated from random locations, and thus they are considered to be representative of the average melt age distribution of the lunar surface. Michael et al. (2018) summarized 94 K–Ar datings of clasts of the lunar highland rocks in lunar meteorites. We refer to the data collectively as K–Ar measurements, although most were made using the Ar–Ar method. These data reflect what can be deconvolved from what is currently available. The histogram (Figure 2(a)) shows that the K–Ar age distribution of the considered meteoritic highland rocks has no prominent peak around 3.9 Ga as is typical for the Apollo highland rocks. Instead, we see a broad and low concentration between 3.7 and 4.4 Ga with three gentle peaks at 3.75, 4.15, and 4.4 Ga.

Comparing the model-derived melt age distribution with the isotopic datings of lunar meteorites suggests that tail-end and sawtooth scenarios match better than the terminal cataclysm scenario regarding the number and magnitude of general peaks.

### 3.2. Distribution at Apollo Sampling Sites

The melt age distribution is spatially varied and shows regional particularity (Liu et al. 2020a). The melt age distribution at sampling sites may thus allow for further constraints on the rate of the early bombardment. Figure 3 shows the integrated melt age distribution of the Apollo sampling sites. Being different from the estimates of the global average, the feature of single sharp peak occurs not only in the terminal cataclysm scenario but also in the sawtooth view. Instead, the melt age distribution under the tail-end impact rate displays a distinctly different pattern, especially for ages >4.1 Ga: in addition to the primary peak at 3.9 Ga, the magnitude of two secondary peaks at 4.25 and 4.35 Ga is significant as well. The distinct features of the estimated distribution of old melt imply that we can use the data of old melt distribution in returned samples to further distinguish between the sawtooth and tail-end scenarios.

The K–Ar dating may not be the most suitable technique to determine the age of old melt products in returned samples. Recent isotopic dating studies concluded that K–Ar datings of Apollo rocks may be biased owing to the resetting of the K–Ar chronometer by subsequent impacts (Fernandes et al. 2013; Michael et al. 2018; Norman et al. 2010). In addition, the old melt products likely experienced extensive impact-induced fracturing, and therefore the grain sizes could be too small to perform reliable K–Ar dating (Liu et al. 2020a; Michael et al. 2018). Instead, the U–Pb datings appear to better conserve

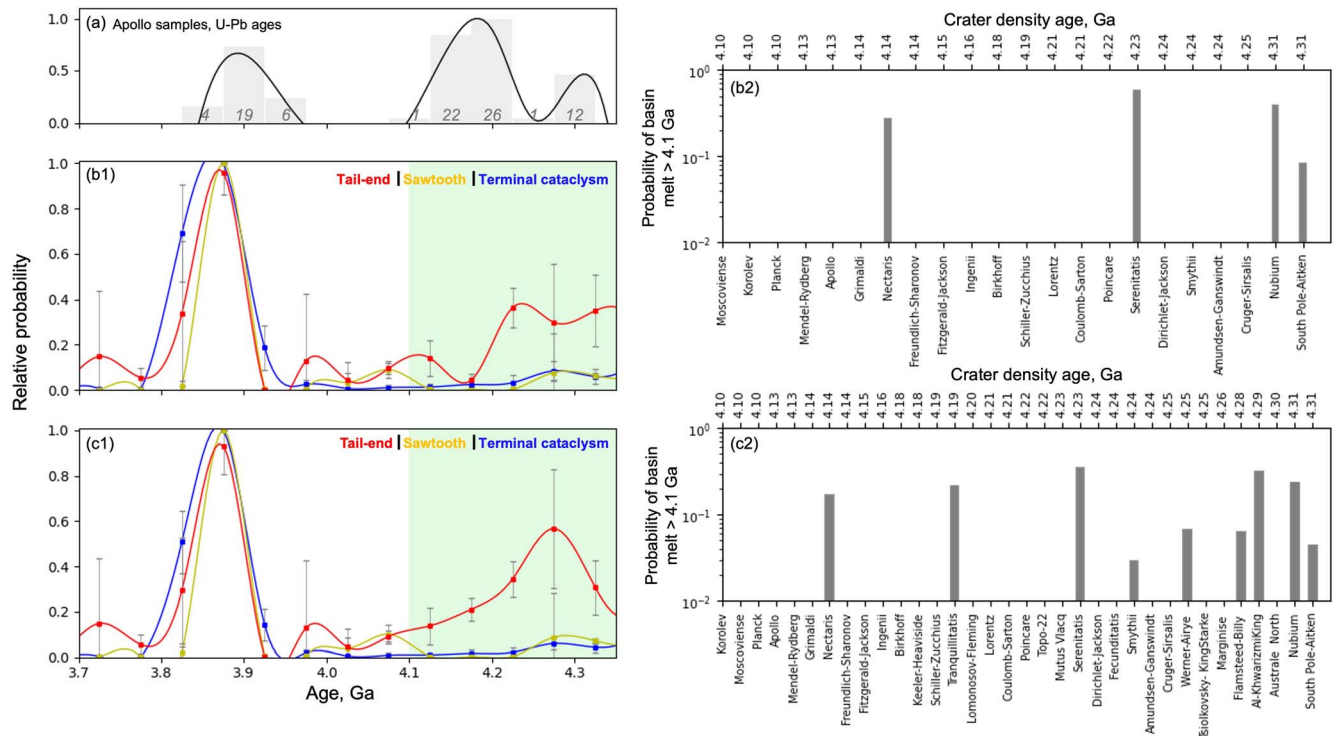


**Figure 3.** Integrated melt age distribution at Apollo sampling sites. (a) U–Pb datings of Apollo 12, 14, 15, 16, 17 samples (Vanderliek et al. 2021), where the black curve is the first-order spline interpolation of the gray histogram. The italic number indicates the number of datings. Panels (b1) and (c1) are the model-derived melt age distributions while considering the basin list of Orgel et al. (2018) and the addition of newly detected pre-Nectarian basins (Conrad et al. 2018), respectively. The considered basins in panel (c1) are 12 more than in panel (b1). The error bars indicate the standard deviation of 10 times Monte Carlo simulations. Their age distribution of basin-sourced melt with an age  $>4.1$  Ga (indicated by the green zones in panels (b1) and (c1)) is shown in panels (b2) and (c2), respectively.

information on the early bombardment history (Crow et al. 2017, and references therein), because the U–Pb zircon chronometer is more robust against resetting by later heating events owing to its high closure temperature and their stability during intense brecciation or moderate heating (Cherniak & Watson 2001), although the lunar zircons that are recording impact ages may have different sources such as melt, altered target rock, or nonmelt ejecta. To assess the current U–Pb age data on zircons of Apollo samples, Vanderliek et al. (2021) compiled  $>1000$  zircon spot analyses from the literature and considered grains of unambiguously impact-related origin. Their results (Figure 3(a)) show that zircons at most landing sites have been affected by impact events between 3.9 and 4.3 Ga (Crow et al. 2017; Joy et al. 2020; Vanderliek et al. 2021), and samples show three impact-related zircon age populations at 3.9, 4.15, and 4.3 Ga.

Compared with the model-derived melt age distribution, as in the globally averaged estimates (Figure 2), the U–Pb data are also difficult to reconcile with the hypothesis of the terminal cataclysm. Note that, in the terminal cataclysm model, a greater number of nonbasin impact events than in the tail-end model is considered. Those nonbasin events generated abundant melt at around 3.85 Ga while remelting some basin melt. However, even under such intensive remelting, the basin-formed  $\sim 3.85$  Ga peak still remains (Figure C1). More importantly, given the distinct patterns of model-derived melt age distribution between the tail-end and the sawtooth scenario (Figure 3), the distribution of the U–Pb data indicates that the modeling results favor the tail-end scenario over the sawtooth.

### 3.3. Influence of Basin Inventory

Finding ancient basins is not trivial since they were heavily degraded by the subsequent impact cratering process. In the recent decades new data became available allowing for the detection of previously unknown ancient basins. Using GRAIL observations, Conrad et al. (2018) derived an updated catalog of lunar ancient basins and estimated their relative ages.

To investigate how the increased number of old basins affects the melt distribution in the near surface and how much of their melt products survive the long-term impact mixing, we also use the updated catalog of lunar basins from Conrad et al. (2018) in our model. Compared with the more conservative catalog of confirmed basins we took into account before (i.e., Orgel et al. 2018), most newly detected basins are old, and they were suggested to be formed in the pre-Nectarian period (Conrad et al. 2018). To derive the absolute crater-derived ages of the newly detected basins, we adopt  $N(20)$  values of Nectaris and SPA basin from Orgel et al. (2018) and assume  $N(20)$  values of newly detected basins to fall in between that of Nectaris and the oldest SPA basin. We assign them random  $N(20)$  values in this range while keeping their relative ages (i.e., the older basins are assigned with a larger  $N(20)$  value). Note that the exact age assignment is not crucial to the arguments stated below, since all these basins are older than mid-pre-Nectarian. As can be seen from Figure 1 (green data), given the assigned  $N(20)$  values, different impact rates result in varying crater-derived ages for these basins. With the additionally considered basins, we calculate the corresponding melt age distribution of the global average and that at the sampling sites. As can be seen from Figure 2(c), regarding the global melt age

distribution, the big picture stays essentially the same, because the majority of melt of the old basins would be deeply buried. The amount remaining in the near surface fills the trough at 4.2 Ga under the tail-end scenario and increases the probability magnitude of 4.5 Ga melt under the sawtooth scenario (Werner 2014). For the terminal cataclysm, the shape of the 3.9 Ga peak holds.

Regarding the melt distribution at the sampling sites (Figure 3(c1)), the estimated melt age distribution for sawtooth and terminal cataclysm stays roughly the same. The significant difference occurs when considering tail-end impact rate, where the 4.2 Ga trough is filled with the melt products of the newly added basins. Based on impact simulations and the constraints on the highly siderophile element budgets of the lunar crust and mantle, Zhu et al. (2019) proposed that many (~90) basins could have formed between 4.15 and 4.35 Ga. The proposed greater number of old basins indicates that the 4.2 Ga peak would be more significant than that shown in Figure 3(c1), which further implies that in the returned samples it is very likely to find more 4.2 Ga melt.

### 3.4. Synthesis of Model-constrained Knowledge on the Timeline of Early Bombardment

Regarding the big picture of the melt age distribution, both the global distribution and regional distribution show that the terminal cataclysm is least consistent with the sample record. In the global distribution, it is hard to evaluate whether the tail-end or the sawtooth scenario matches the observed record better since both display comparable features. But in the regional distribution of the Apollo sampling sites, the melt distributions of the tail-end and sawtooth scenarios show distinct features, where the tail-end seems to better agree with the sample record. If the applied sample data are representative of the general melt age distribution on the Moon, the modeling results suggest a tail-end scenario for the impact rate of the early bombardment history.

## 4. Abundance of Nectaris Melt in Apollo-returned Samples

The age of the Nectaris basin marks the beginning of the Nectarian period and is essential for the lunar geologic timescale. Determining Nectaris age can also provide essential constraints on the impact rate of the early bombardment. However, due to the difficulty in interpreting the sample origin, the age of the Nectaris basin is still debated. Some lunar samples from Apollo 16 might be Nectaris ejecta, but they have so far not been tied convincingly to that basin. The often-quoted ages of 3.92 Ga for Nectaris (Stöffler & Ryder 2001) tend to favor a terminal cataclysm, whereas an older age of Nectaris >4.1 Ga would weaken such a hypothesis (Fischer-Gödde & Becker 2011).

Given the model-derived most plausible timeline of early bombardment having a tail-end shape, Nectaris tends to have an age older than ~4.1 Ga. Estimating the distribution of basin-sourced melt with ages >4.1 Ga can thus help to constrain the probability of the presence of Nectaris melt in the returned samples. In Figure 3, we calculate the distribution of basin-sourced melt >4.1 Ga (in the top 5 m) in the tail-end impact rate. When only confirmed basins are considered (i.e., Orgel et al. 2018), Nectaris, Serenitatis, Nubium, and SPA are the major contributors of basin-sourced melt. Except for Serenitatis, Nectaris is the primary source of ~4.1–4.2 Ga melt. When

newly detected basins are considered (Conrad et al. 2018), as expected, the old melt could derive from numerous basins. In the melt of ~4.1–4.2 Ga, Nectaris is one of three major contributors (Nectaris, Tranquilitatis, and Serenitatis), and its melt accounts for about 25%. Note that the above discussions are based on our modeling results. Sample ages are determined from breccia that have a wide spread of ages.

## 5. Presence of Pre-Nectarian Melts in the Near-surface Materials

Although it is difficult to identify ancient basins owing to their heavily degraded structure, evidence of their formation could have remained in their melt products. However, the older the melts, the more intensive the impact mixing they have experienced, which makes their spatial distribution complicated. In addition, identifying whether the old components in the samples are the products of basin-forming events is key to making connections with the early bombardment history, which has also been found to be difficult during sample interpretations (Stöffler & Ryder 2001). To constrain the abundance of old melt, in Figure 4 we calculated the present-day abundance of pre-Nectarian melts in the near surface considering different basin inventories. Regardless of the number of basins, the majority of old melts were reheated or deeply buried, and only a small amount remains on the surface. Inside and near the basin cavities the strata are enriched with impact melt, but the residuum over regions far away is scarce, where the majority of the melts are buried to a depth >100 m (Liu et al. 2021). Except for the melt-enriched zones, the near surface contains less than 3% pre-Nectarian melt. Almost all the sampling sites are close to the basin cavities, indicating that abundant ancient melt should be contained in the existing samples.

## 6. Discussions and Conclusions

To constrain the timeline of the early lunar bombardment, we investigate the outcome of melt age distribution assuming three types of impact rate decay scenarios: tail-end, sawtooth, and terminal cataclysm. These scenarios are individually taken into account in the spatial-resolved impact mixing model. We estimate the model-derived present-day melt age distribution both of the global average and at the Apollo sampling sites. The former is compared with the present data of lunar meteorites and the latter with Apollo samples. The K–Ar age distribution of lunar meteorites displays three gentle peaks between 3.7 and 4.5 Ga, which is consistent with the model-derived global average of melt age distribution for both the tail-end and sawtooth scenarios and is inconsistent with that of a terminal cataclysm, where only one sharp peak appears. The U–Pb age distribution of Apollo samples shows significant contributions of impact melt older than 4.1 Ga, with two peaks at 4.15 and 4.3 Ga, where the model-derived melt age distribution fits best with a tail-end scenario. In summary, these results suggest that if the applied sample data are representative of the general melt age distribution on the Moon, the timeline of early bombardment most likely corresponds to the shape of a tail-end scenario. A sawtooth scenario cannot be ruled out; the terminal cataclysm is least likely.

The preservation state of the SPA basin implies that it was formed after the crust formation or at least at the late stage of the solidification of the lunar magma ocean (LMO), when most



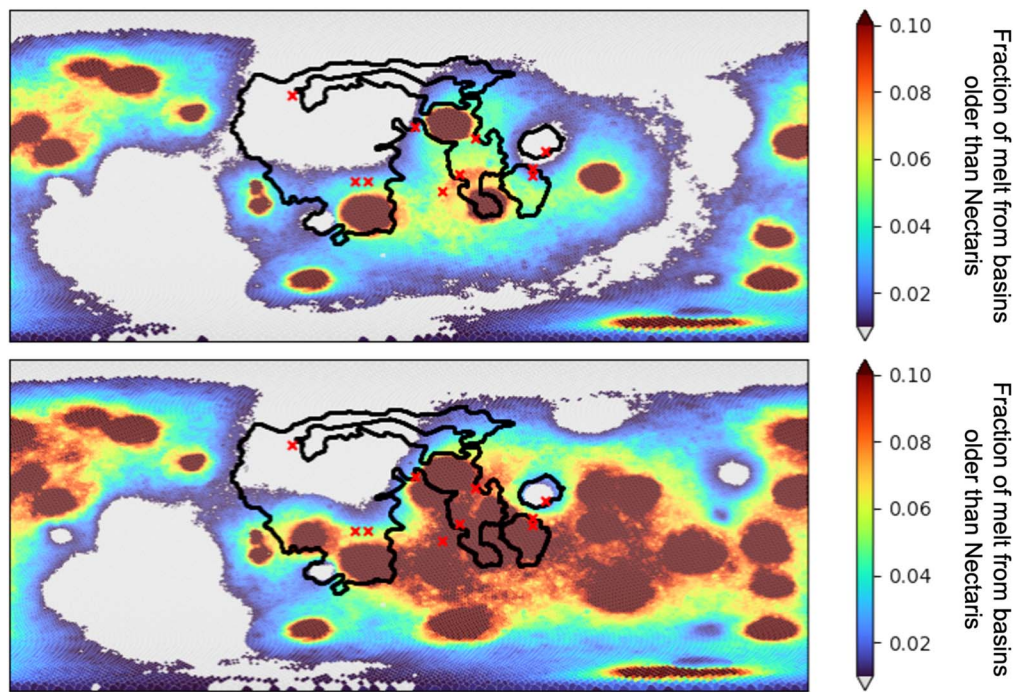


**Figure 4.** Abundance of pre-Nectarian melt relative to all the materials in the top 5 m when considering the basin list of Orgel et al. (2018; top panel) and an addition of newly detected pre-Nectarian basins (Conrad et al. 2018; bottom panel). Abundances below 0.01 are shown in gray, and those above 0.10 are shown in dark red. The red crosses point out the location of so-far-accomplished sample return missions (Chang’e-5, Apollo, and Luna). The black curves outline the boundary of maria where the surface has been filled with volcanic materials.

of the magma was solidified. During the main phase of LMO crystallization (Elkins-Tanton et al. 2011), impacts should have failed to produce long-lasting structures owing to the low viscosity of the warm crust and mantle (Kamata et al. 2015). The SPA crater-derived age is 4.3, 4.5, and 3.85 Ga assuming the tail-end, sawtooth, and cataclysm scenario, respectively (Figure 1). The distinct ages correspond to varying solidification timescales of the LMO. Assuming that the Moon was formed about 4.5 Ga ago (Kruijjer & Kleine 2017) and the SPA is the oldest basin on the Moon (Garrick-Bethell & Zuber 2009), the model-supported tail-end scenario suggests an extended solidification timescale for the LMO of about 150–200 Ma after lunar formation (Maurice et al. 2020).

The various scenarios of early bombardment likely imply different sources of impactors during late accretion. In a tail-end scenario, the impactors originate from the same planetesimal population as those of the main accretion phase. By contrast, any abrupt increase in the impact rate including both the terminal cataclysm and sawtooth scenarios possibly requires a dynamical event that destabilized the planetesimal disk and led to a sudden surge in the influx of impactors, originating from (1) the cometary disk (Gomes et al. 2005), (2) the primordial main asteroid belt (Marchi et al. 2013), and/or (3) the E-belt (Morbidelli et al. 2012). Different sources of impactors have distinct isotopic features. In case 1, we would expect the lunar impactites to have carbonaceous (CC)-like isotope signatures with only little contribution from noncarbonaceous (NC) material. In case 2, we could see an isotopically anomalous, potentially mixed NC–CC signature in the lunar impactites. In case 3, the lunar impactites may have enstatite-chondrite-like isotope signatures. Recently, based on genetically characteristic ruthenium and molybdenum isotope compositions of lunar-impact-derived rocks, Worsham & Kleine (2021) found that the impactors during the entire period

of late accretion have the same type of bodies, supporting the tail-end timeline during the late accretion phase. In addition, different sources of impactor populations would be expected to translate into a change in the crater PF between the oldest lunar terrains and those occurring near the impact influx surge. Several authors have suggested that the shape of the PF changed over time, suggesting different impactor populations (Strom et al. 2005; Head et al. 2010; Bottke et al. 2012). Using an improved crater counting technique, the buffered nonsparseness correction technique that takes crater obliteration into account, Orgel et al. (2018) reinvestigate the crater populations of 30 lunar basins. They found no difference in the shapes of the crater size–frequency distribution (i.e., PF) of pre-Nectarian, Nectarian, and Imbrian basins, supporting no change in impactor population.

A robust test of the late cataclysm hypothesis will require an accurate absolute age for the older lunar basins. A stratigraphically intermediate basin, such as Nectaris, may serve as a diagnostic test of the cataclysm. An older age of  $>4.1$  Ga would weaken the scenario of a cataclysm. In addition, the SPA basin is stratigraphically the oldest preserved basin on the Moon, and its age would provide strong evidence for a terminal cataclysm if it is very young (i.e.,  $\sim 4$  Ga; Norman 2009). Quantitative ages for these basins would vastly improve our understanding of the early impact history.

The model-favored form of the early bombardment being tail-end corresponds to a Nectaris age earlier than 4.1 Ga. To help in interpreting old basin melt in the returned samples, we estimate the probability of Nectaris melt in  $>4.1$  Ga melt at the Apollo sampling sites. The results indicate a high probability of  $\sim 4.2$  Ga melt in samples being derived from the Nectaris basin. Even if a greater number of ancient basins is considered, the Nectaris melt should still account for about 25% of  $>4.1$  Ga melt of the Apollo samples. We then present the spatial

distribution of pre-Nectarian melt over the global surface. The old melt is found to be generally scarce at the surface, but inside and near basin cavities higher abundances may be found. For most of the regions, the old melt is buried to a depth  $> 100$  m. This indicates that for the future mission to collect pre-Nectarian melts, the collected surface materials are ideally derived from the excavation of impact craters at least 1 km in diameter. In addition, the surface materials in roughly the top 10 cm would have experienced intensive gardening by smaller impacts, leading to the excess of impact melt  $< 0.5$  Ga. In the greater depths, impact melts from larger impacts and basin-forming events still dominate (Liu et al. 2021). Therefore, fresh excavated materials would be preferred targets.

### Acknowledgments

We greatly appreciate two anonymous reviewers for insightful reviews that improved the quality of the manuscript. This work was funded by the Deutsche Forschungsgemeinschaft (SFB-TRR 170/2), publication No. 185. All data to reproduce the figures in this work can be accessed in TRR170-DB at doi:10.35003/SYA4DC.

### Appendix A

#### Monte Carlo Impact Mixing Model

We use the Monte Carlo method to simulate the impact mixing process. Three types of impact rate functions (tail-end, Neukum 1983; terminal cataclysm, Tera et al. 1974; sawtooth, Morbidelli et al. 2012) are applied to calculate the occurrence time of impacts. The minimum crater diameter considered is chosen as 5 km. The size–frequency distribution of generated craters (CSFD) conforms to the PF (Neukum 1983). The CSFD of different scenarios is shown in Figure A1. All the craters are randomly distributed over the surface except for the impact basins. To better constrain the evolution of basin melt abundance, they occur according to a table of the actual lunar basins. At first, 30 basin-forming events, the crater populations of which were reinvestigated using the buffered nonsparseness correction technique, are included in our simulations (Orgel et al. 2018). The buffered nonsparseness correction technique takes crater obliteration into account for the superposed crater densities, providing more accurate measurements of the occurrence times of basins (Riedel et al. 2018). To investigate the influence of varying inventory of basins on the melt age distribution, we then add newly detected ancient basins from Conrad et al. (2018; see Table B1).

In the model, for each impact formation event, we simulate the process of melting (remelting), excavation, and ejecta deposition. An excavation depth,  $d_{\text{exc}}$ , is approximated to be one-third of the transient crater depth,  $d_t$ , which corresponds to 1/10 of the transient crater diameter ( $D_t$ ). The transient crater diameter is related to the morphology of the final crater: for simple craters,  $D_t = 0.8D$  (Melosh 1989), where  $D$  is the rim-to-rim distance of final craters; for complex craters,  $D_t = (DD_Q^{0.13}/1.17)^{1/1.13}$  (McKinnon et al. 1997), where  $D_Q$  is the simple–complex transition diameter and is taken as 21 km (Pike 1977). Both scaling laws used to calculate  $D_t$  do not extrapolate well to basin sizes. Recently, Miljković et al. (2016) calculated the basins  $D_t$  using both the high-resolution GRAIL-derived crustal thickness maps and the iSALE hydrocode numerical modeling. We use the estimates of Miljković et al. (2016) for our basin  $D_t$ . For the basins whose

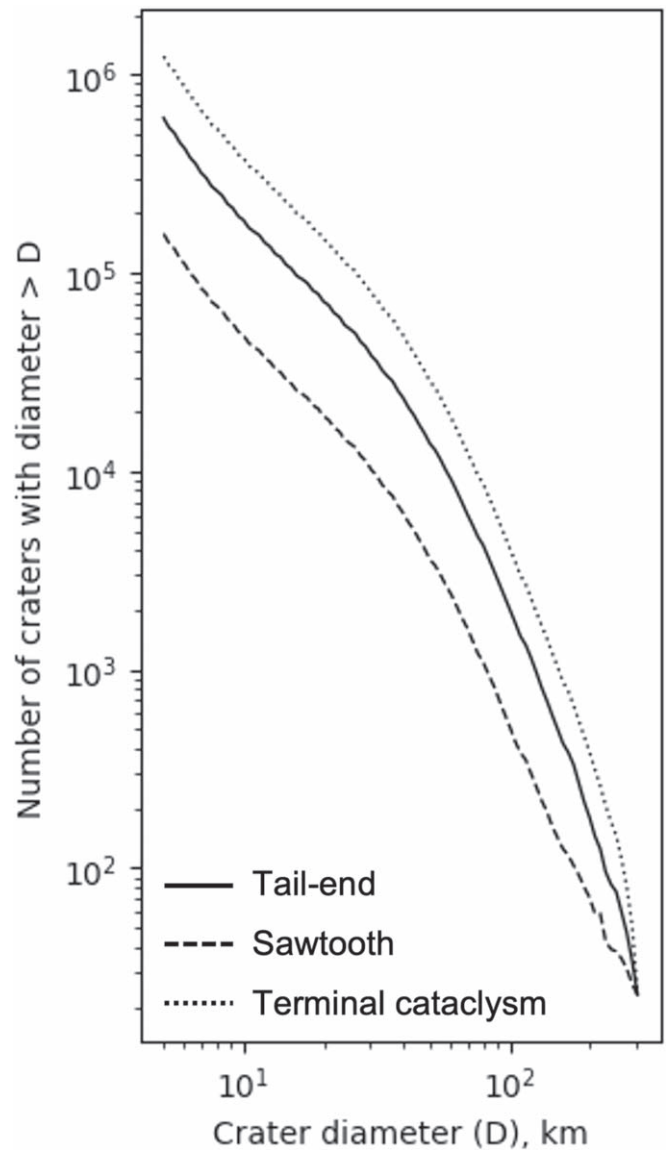


**Figure A1.** Cumulative number of generated craters considering impact rate function of tail-end, sawtooth, and terminal cataclysm.

$D_t$  was not contained in Miljković et al. (2016), we adopt the measurements from Wieczorek & Phillips (1999), where the transient basin size was determined using gravity models. We calculate a linear fit between the measured  $D$  and  $D_t$ , which is applied for basins whose  $D_t$  is not considered in both studies. As can be seen from Figure A2, the unknown  $D_t$  is estimated according to their  $D$  measurements (red circles).

The volume of the excavated materials,  $V_{\text{exc}}$ , is estimated to be 1/3 of a disk with  $d_{\text{exc}}$  in thickness and  $D_t$  in diameter. The total volume of the generated impact melts with a reset age as the current model time is  $V_{\text{melt}} = 1.4 \times 10^{-4} D_t^{3.85}$  (Cintala & Grieve 1998). About 75% of  $V_{\text{melt}}$  stays inside the crater, and about 25% of  $V_{\text{melt}}$  is ejected (Liu et al. 2020a, 2022a). Although the slope of the scaled  $V_{\text{melt}}$  is found to be sensitive to the  $D_t$  measurement (Liu et al. 2022a), the nature that the basin  $V_{\text{melt}}$  is greater than that of smaller impacts by several orders of magnitudes holds.

The majority of excavated materials deposit within 2–3 radii from the crater center in the form of ejecta blankets, which are followed by patchy zones spanning about three radii. Continual



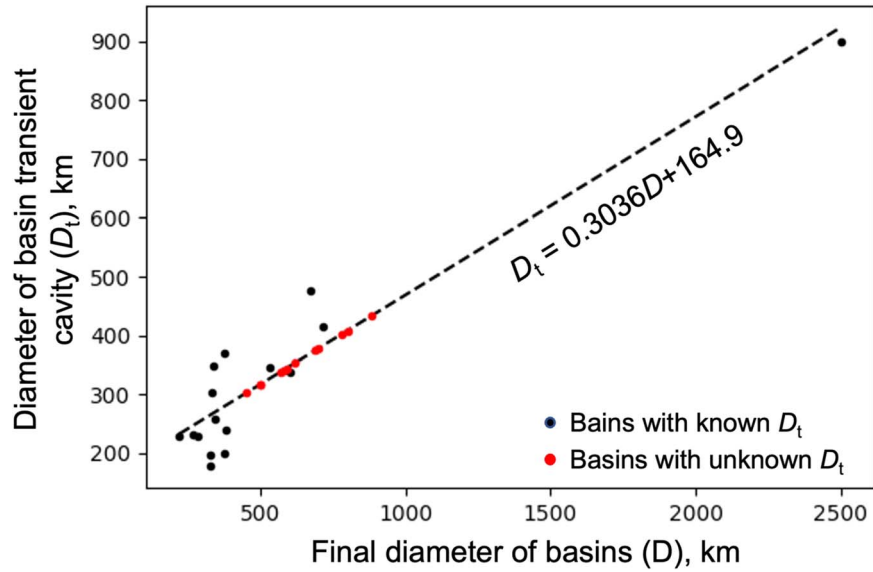


**Figure A2.** Distribution of basin  $D$  and  $D_t$ , where the known  $D_t$  (black circles) is derived from Miljković et al. (2016) and Wieczorek & Phillips (1999). The unknown  $D_t$  (red circles) is estimated based on a linear fit of the known  $D$  and  $D_t$  (black circles).

ejecta blankets and patchy zones encompass most of the total ejecta (about 85%). For proximal ejecta, the thickness of ejecta layers,  $\delta$ , decreases with distance from crater center,  $r$  (Melosh 1989):

$$\delta(r) = Ar^{-3}, \quad (\text{A1})$$

where  $A$  varies for differently sized craters to conserve mass and is calculated by taking the integrated volume exactly to be  $V_{\text{exc}}$ . Although the volume of distal ejecta is not large, previous studies have shown its significance (Liu et al. 2022a). In this model, we trace the melt within 10 radii. To estimate the distribution of distal ejecta, we assume that it is also continuously distributed, and the thickness is calculated based on the extrapolated power law mentioned above. Although, initially, the distal ejecta is not distributed continuously, with continuous impact mixing the patchy distal ejecta would fade into the background, and the thickness distribution becomes more uniform. The average effect on distal ejecta looks similar to a uniform distribution.

For the melt distribution in ejected materials, we calculate the melt thickness  $\delta_m$  of a hypothetical “melt blanket,” which only consists of impact melt material. The thickness of melt,  $\delta_m$ , also decreases with  $r$  but with a shallower slope (Liu et al. 2022a):

$$\delta_m(r) = A_m r^{-2.2}. \quad (\text{A2})$$

Note that melt in the ejecta does not occur as a distinct layer but is distributed over the entire thickness of the ejecta layer.  $\delta_m(r)/\delta(r)$  represents the melt content in the ejecta layer at a given distance  $r$ . Similar to  $A$ ,  $A_m$  also varies for different-sized craters and is estimated by taking the integrated volume within 10 radii exactly to be the melt volume that is ejected from the cavity.

To record the evolving melt component, the model uses cells that are nearly uniformly distributed on a sphere. This simplifies the calculation of the integrated ejecta volume over the spherical body and avoids the bias caused by the surface curvature. Assuming a total of  $10^6$  cells on the lunar surface, the spheroidal coordinates of the  $i$ th cell  $(x_i, y_i, z_i)$  can be obtained using the Fibonacci lattice (González 2010):

$$\begin{cases} z_i = R(2i - 1)/N - R \\ x_i = \sqrt{R^2 - z_i^2} \cos(2\pi i \varnothing), \\ y_i = \sqrt{R^2 - z_i^2} \sin(2\pi i \varnothing) \end{cases} \quad (\text{A3})$$

where  $R$  is the radius of the Moon and  $\varnothing = (\sqrt{5} - 1)/2 \approx 0.618$ , the golden ratio. Each cell is related to a certain area for which the melt age distribution is tracked.

## Appendix B

A list of basins considered in the model is given in Table B1.

**Table B1**  
List of Basins Considered in the Model

Name <sup>a</sup>	Longitude (deg)	Latitude (deg)	<i>D</i> (km)	<i>N</i> (20) <sup>b</sup>	Relative Age <sup>c</sup>
South Pole– Aitken	–169	–53	2500	254	...
Nubium	–17.29	–20.59	714.5	526	...
<i>Australe North</i>	96	–35.5	880	...	PN2
<i>Al-Khwar- izmi–King</i>	11	21	590	...	PN2
<i>Flansteed –Billy</i>	–45	–7.5	570	...	PN2
<i>Marginise</i>	84	20	580	...	PN2
<i>Tsiolkovsky– King–Starke</i>	128	–15	700	...	PN2
<i>Werner–Airye</i>	12	–24	500	...	PN2
Cruger–Sirsalis	–67	–16	268	365	...
Amundsen –Ganswindt	123	–81	380	359	...
Smythii	87.05	–1.71	374	355	...
<i>Fecunditatis</i>	52	–4	690	...	PN3
Dirichlet –Jackson	–158	13	220	346	...
Serenitatis	18.36	27.29	674	334	...
<i>Mutus Vlacq</i>	24	–53.5	450	...	PN3
<i>Topo-22</i>	179	49.9	500	...	PN3
Poincare	163.99	–56.86	346	286	...
Coulomb –Sarton	–123	52	530	281	...
Lorentz	–97.19	34.59	378	275	...
<i>Lomonosov –Fleming</i>	105	19	620	...	PN3
<i>Tranquillitatis</i>	40	7	800	...	PN3
Schiller –Zucchius	–45	–56	325	234	...
<i>Keeler –Heaviside</i>	162	–10	780	...	PN4
Birkhoff	–145.65	58.45	329.8	223	...
Ingenii	164.83	–33.25	282.2	198	...
Fitzgerald –Jackson	–170	25	334	184	...
Freundlich –Sharonov	176	19	600	173	...
Nectaris	34.6	–15.19	339	172	...
Grimaldi	–68.36	–5.38	173	165	...
Mendel –Rydberg	–94	–50	420	158	...
Apollo	–151.48	–35.69	524	158	...
Planck	135.34	–57.27	319	135	...
Moscoviense	148.12	27.28	276	128	...
Korolev	–157.41	–4.19	423	128	...
Mendeleev	141.17	5.38	325	125	...
Humorum	–38.57	–24.48	419	121	...
Hertzprung	–128.66	1.37	536	116	...
Crisium	59.1	16.18	556	114	...
Humboldtianum	81.54	56.92	231	109	...
Imbrium	–14.91	34.72	1146	26	...
Oriente	–94.67	–19.87	294	20	...
Schrödinger	132.97	–74.73	316	19	...

#### Notes.

<sup>a</sup> The basins in roman font have measured crater density by Orgel et al. (2018), and those in italic font are newly detected ancient basins having only relative ages (Conrad et al. 2018). Note that there are other sequences of event lists (e.g., Baldwin 1974; Wilhelms 1987; Fassett et al. 2012), and we consider the recently updated one since it was obtained using better observation data and took crater obliteration into account, thus providing more accurate measurements for crater-derived ages.

<sup>b</sup> Orgel et al. (2018).

<sup>c</sup> Conrad et al. (2018) Pre-Nectarian 1 (PN1) contains the oldest known basin. As the subperiod gets younger, the number counts go up (e.g., PN3 is younger than PN2).

## Appendix C

Basin and nonbasin impact melt at the Apollo sampling sites are shown in Figure C1.

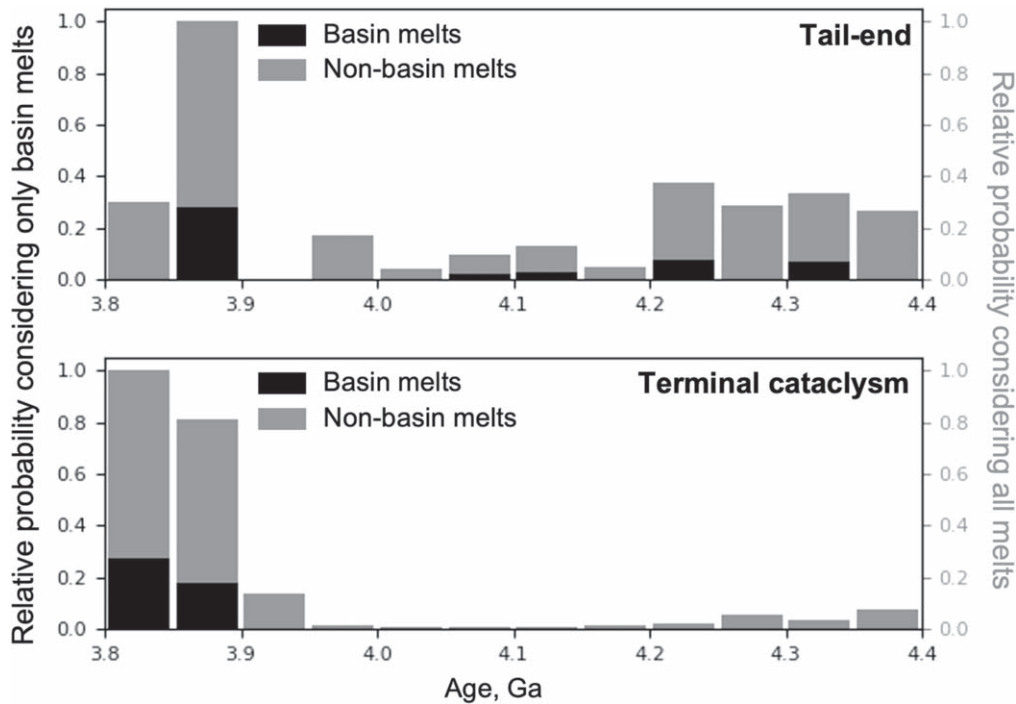


**Figure C1.** Age distribution of basin and nonbasin impact melt at the Apollo sampling sites in the top 5 m.

### ORCID iDs

Tiantian Liu  <https://orcid.org/0000-0002-1539-495X>

### References

- Baldwin, R. B. 1974, *Icar*, **23**, 97
- Boehnke, P., & Harrison, T. M. 2016, *PNAS*, **113**, 10802
- Boehnke, P., Harrison, T. M., Heizler, M. T., & Warren, P. H. 2016, *E&PSL*, **453**, 267
- Bottke, W. F., Vokrouhlický, D., Minton, D., et al. 2012, *Natur*, **485**, 78
- Chapman, C. R., Cohen, B. A., & Grinspoon, D. H. 2007, *Icar*, **189**, 233
- Cherniak, D. J., & Watson, E. B. 2001, *ChGeo*, **172**, 5
- Cintala, M. J., & Grieve, R. A. F. 1998, *M&PS*, **33**, 889
- Cohen, B. A. 2000, *Sci*, **290**, 1754
- Conrad, J. W., Nimmo, F., Fassett, C. I., & Kamata, S. 2018, *Icar*, **314**, 50
- Crow, C. A., McKeegan, K. D., & Moser, D. E. 2017, *GeCoA*, **202**, 264
- Elkins-Tanton, L. T., Burgess, S., & Yin, Q.-Z. 2011, *E&PSL*, **304**, 326
- Fassett, C. I., Head, J. W., Kadish, S. J., et al. 2012, *JGRE*, **117**, E00H061
- Fernandes, V. A., Fritz, J., Weiss, B. P., Garrick-Bethell, I., & Shuster, D. L. 2013, *M&PS*, **48**, 241
- Fischer-Gödde, M., & Becker, H. 2011, *LPSC*, **42**, 1414
- Garrick-Bethell, I., & Zuber, M. T. 2009, *Icar*, **204**, 399
- Gomes, R., Levison, H. F., Tsiganis, K., & Morbidelli, A. 2005, *Natur*, **435**, 466
- González, Á. 2010, *MaGeo*, **42**, 49
- Hartmann, W. K. 2003, *M&PS*, **38**, 579
- Haskin, L. A., Korotex, R. L., Rockow, K. M., & Jolliff, B. L. 1998, *M&PS*, **33**, 959
- Head, J. W., Fassett, C. I., Kadish, S. J., et al. 2010, *Sci*, **329**, 1504
- Huang, Y., Minton, D. A., Masatoshi, H., et al. 2017, *JGRE*, **122**, 1158
- Ivanov, B. A. 2001, *SSRv*, **96**, 87
- Joy, K. H., Snape, J. F., Nemchin, A. A., et al. 2020, *RSOS*, **7**, 200236
- Kamata, S., Sugita, S., Abe, Y., et al. 2015, *Icar*, **250**, 492
- Kruijer, T. S., & Kleine, T. 2017, *E&PSL*, **475**, 15
- Liu, T., Luther, R., Manske, L., & Wünnemann, K. 2022a, *JGRE*, **127**, e2022JE007264
- Liu, T., Michael, G., Haber, T., & Wünnemann, K. 2021, *JGRE*, **126**, e2020JE006708
- Liu, T., Michael, G., Wünnemann, K., Becker, H., & Oberst, J. 2020a, *Icar*, **339**, 113609
- Liu, T., Michael, G., Zuschneid, W., Wünnemann, K., & Oberst, J. 2020b, *Icar*, **358**, 114206
- Liu, T., Wünnemann, K., & Michael, G. 2022b, *E&PSL*, **597**, 117817
- Marchi, S., Bottke, W. F., Cohen, B. A., et al. 2013, *NatGe*, **6**, 303
- Marchi, S., Bottke, W. F., Kring, D. A., & Morbidelli, A. 2012, *E&PSL*, **325**, 27
- Maurice, M., Tosi, N., Schwinger, S., Breuer, D., & Kleine, T. 2020, *SciA*, **6**, eaba8949
- McKinnon, W. B., Zahnle, K. J., Ivanov, B. A., & Melosh, H. J. 1997, in *Venus II: Geology, Geophysics, Atmosphere, and Solar Wind Environment*, ed. S. W. Bougher, D. M. Hunten, & R. J. Phillips (Tucson, AZ: Univ. Arizona Press), 969
- Melosh, H. J. 1989, in *Impact Cratering: A Geologic Process*, ed. G. Michael, A. Basilevsky, & G. Neukum (New York: Oxford Univ. Press), 80
- Michael, G., Basilevsky, A., & Neukum, G. 2018, *Icar*, **302**, 80
- Michael, G., & Neukum, G. 2010, *E&PSL*, **294**, 223
- Miljković, K., Collins, G. S., Wieczorek, M. A., et al. 2016, *JGRE*, **121**, 1695
- Morbidelli, A., Marchi, S., Bottke, W. F., & Kring, D. A. 2012, *E&PSL*, **355**, 144
- Neukum, G. 1983, Habilitation Dissertation for Faculty Membership, Univ. Munich
- Norman, M. D. 2009, *Elme*, **5**, 23
- Norman, M. D., Duncan, R. A., & Huard, J. J. 2006, *GeCoA*, **70**, 6032
- Norman, M. D., Duncan, R. A., & Huard, J. J. 2010, *GeCoA*, **74**, 763
- Orgel, C., Michael, G., Fassett, C. I., et al. 2018, *JGRE*, **123**, 748
- Pike, R. J. 1977, *LPSC*, **3**, 3427
- Riedel, C., Michael, G., Kneissl, T., et al. 2018, *E&SS*, **5**, 258
- Robbins, S. J. 2014, *E&PSL*, **403**, 188
- Schaeffer, G. A., & Schaeffer, O. A. 1977, *LPSC*, **2**, 2253
- Stöffler, D. 2006, *RvMG*, **60**, 519
- Stöffler, D., & Ryder, G. 2001, in *Chronology and Evolution of Mars*, ed. R. Kallenbach, J. Geiss, & W. K. Hartmann (Dordrecht: Springer), 9
- Strom, R. G., Malhotra, R., Ito, T., Yoshida, F., & Kring, D. A. 2005, *Sci*, **309**, 1847



- Tera, F., Papanastassiou, D. A., & Wasserburg, G. J. 1973, *LPSC*, **4**, 723  
Tera, F., Papanastassiou, D. A., & Wasserburg, G. J. 1974, *E&PSL*, **22**, 1  
Tsiganis, K., Gomes, R., Morbidelli, A., & Levison, H. F. 2005, *Natur*, **435**, 459  
Vanderliek, D. M., Becker, H., & Rocholl, A. 2021, *E&PSL*, **576**, 117216  
Vogt, S., Fink, D., Klein, J., et al. 1991, *GeCoA*, **55**, 3157  
Warren, P. H. 1994, *Icar*, **111**, 338  
Werner, S. C. 2014, *E&PSL*, **400**, 54  
Wieczorek, M. A., & Phillips, R. J. 1999, *Icar*, **139**, 246  
Wilhelms, D. E. 1987, *The Geologic History of the Moon*, U.S. Geological Survey Professional Paper 1348  
Worsham, E. A., & Kleine, T. 2021, *SciA*, **7**, eabh2837  
Zhu, M.-H., Artemieva, N., Morbidelli, A., et al. 2019, *Natur*, **571**, 226  
Zhu, M.-H., Wünnemann, K., & Artemieva, N. 2017, *GeoRL*, **44**, 11292